Eur. Phys. J. D **12**, 33–44 (2000)

THE EUROPEAN PHYSICAL JOURNAL D

EDP Sciences

Isotope shifts and hyperfine structure in calcium 4snp $^1P_1$ and 4snf F Rydberg states

P. Müller[1], B.A. Bushaw[2,a], W. Nörtershäuser[2], and K. Wendt[1]

[1] Institut für Physik, Johannes Gutenberg-Universität Mainz, 55099 Mainz, Germany
[2] Pacific Northwest National Laboratory, Richland, WA 99352, USA

Received 17 December 1999 and Received in final form 29 March 2000

Abstract. Isotope shifts and hyperfine structure have been measured in $4snp\ ^1P_1$ and $4snf$ F Rydberg states for all stable calcium isotopes and the radioisotope ^{41}Ca using high-resolution laser spectroscopy. Triple-resonance excitation *via* $4s^2\ ^1S_0 \rightarrow 4s4p\ ^1P_1 \rightarrow 4s4d\ ^1D_2 \rightarrow$ *Rydberg state* was followed by photoionization with a CO_2 laser and mass selective ion detection. Isotope shifts for the even-mass isotopes have been analyzed to derive specific mass shift and field shift factors. The apparent isotope shifts for ^{41}Ca and ^{43}Ca exhibit anomalous values that are n-dependent. This is interpreted in terms of hyperfine-induced fine-structure mixing, which becomes very pronounced when singlet-triplet fine-structure splitting is comparable to the hyperfine interaction energy. Measurements of fine-structure splittings for the predominant isotope ^{40}Ca have been used as input parameters for theoretical calculation of the perturbed hyperfine structure. Results obtained by diagonalizing the second-order hyperfine interaction matrices agree very well with experimentally observed spectra. These measurements allow the evaluation of highly selective and sensitive methods for the detection of the rare ^{41}Ca isotope.

PACS. 32.10.Fn Fine and hyperfine structure – 32.80.Rm Multiphoton ionization and excitation to highly excited states (*e.g.*, Rydberg states)

1 Introduction

In recent years we have been developing methods for the sensitive and selective ultratrace detection of calcium isotopes using resonance ionization mass spectrometry (RIMS). The most demanding application is the detection of the long-lived radioisotope ^{41}Ca ($t_{1/2} = 1.04 \times 10^5$ a) for radiodating of geologic and anthropologic samples [1], where the abundance of ^{41}Ca is expected to be only 10^{-16} to 10^{-14} with respect to the predominant stable isotope ^{40}Ca. Enriched ^{41}Ca has also been used as a medical tracer for investigation of calcium metabolism in the human body [2], and its abundance in meteorites can reveal information about the age and radiation history of the material [3]. In both cases, ^{41}Ca/^{40}Ca ratios are on the order of 10^{-10} to 10^{-12}. In general, extremely high isotopic selectivity is required to suppress the vast excess of the neighboring ^{40}Ca. Previously, we studied both single-resonance $4s^2\ ^1S_0 \rightarrow 4s4p\ ^1P_1$ (A in Fig. 1) and double-resonance $4s^2\ ^1S_0 \rightarrow 4s4p\ ^1P_1 \rightarrow 4s4d\ ^1D_2$ (B in Fig. 1) excitation of calcium, followed by subsequent photoionization with an argon-ion laser. These investigations included measurement of isotope shifts (IS) and, where applicable, hyperfine structure (HFS) for all six stable calcium isotopes and for ^{41}Ca in both transitions [4]. Additionally, the lineshapes of the optical resonances have been examined extensively and a theoretical model using the density matrix formalism has been developed for accurately calculating these profiles [5]. The results of these investigations revealed that, with double-resonance excitation,

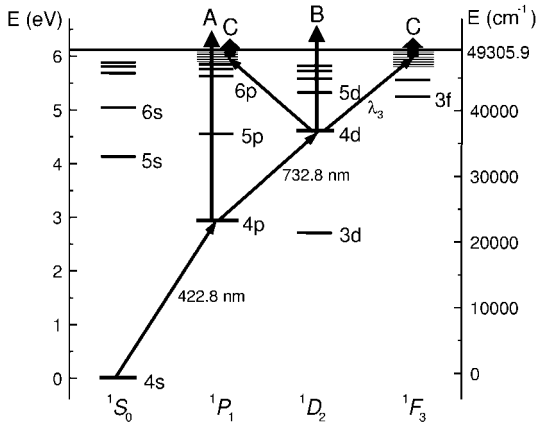

Fig. 1. Partial energy level diagram for calcium showing excitation pathways for (A) single-, (B) double-, and (C) triple-resonance ionization.

[a] e-mail: bruce.bushaw@pnl.gov

the ^{41}Ca/^{40}Ca optical selectivity is limited to $\sim 10^5$ and overall detection efficiency is $\sim 10^{-6}$. Both these values are not sufficient for most of the targeted applications. However, extended theoretical calculations with the density matrix model have indicated that a third resonant excitation to a Rydberg state will further narrow the lineshape and, when combined with a third set of isotope shifts, should lead to much higher optical isotopic selectivity [6]. Additionally, photoionization out of a Rydberg state can be very efficient using a CO_2 laser [7]. Thus, it is expected that triple-resonance excitation should improve both optical selectivity and ionization efficiency several orders of magnitude over the previously studied double-resonance approach.

Building on the double-resonance excitation and starting in the $4s4d\ ^1D_2$ intermediate state, third resonant transitions are allowed only to members of the $4snp\ ^1P_1$ and $4snf\ ^1F_3$ Rydberg series (C in Fig. 1). While the even-parity $^1S_0$ and $^1D_2$ Rydberg series of calcium have been investigated previously at high resolution [8–10], to our knowledge, the IS and HFS in the $^1P_1$ and $^1F_3$ Rydberg series have not yet been studied. In this paper, we report on measurements of IS and HFS in these series for all stable, naturally occurring isotopes of calcium. Measurements have also been performed for ^{41}Ca in the $4snf\ ^1F_3$ series. For the even-mass isotopes, the observed IS are nearly constant. However, beyond the small normal mass shifts expected for the slightly different energies of the Rydberg states, there is a n-dependent change in the specific mass shift in the $4snp\ ^1P_1$ series, indicating that there is still significant interaction of the Rydberg electron with the core. In contrast, the odd-mass isotopes ^{41,43}Ca exhibit anomalous IS and perturbed HFS that are strongly n-dependent. These effects are much more pronounced in the $^1F_3$ series and are similar to anomalous IS [11,12] and perturbed HFS [13] reported for the system of $5sns$ Rydberg states in ^{87}Sr, both of which were attributed to hyperfine-induced singlet-triplet mixing. More recently, analogous effects were observed in a few states of the $5snf$ F Rydberg series of strontium [14]. These were also interpreted in terms of hyperfine-induced fine-structure mixing (HFM); however, all four members of the fine-structure multiplet had to be considered to yield a proper description of the observed spectra. This type of complex level interaction occurred only for isotopes with non-zero nuclear spin, ^{87}Sr and ^{89}Sr [15], and became particularly pronounced when the fine-structure splittings were comparable to the hyperfine interaction energy. In this paper, we apply a similar HFM analysis to the current measurements on calcium. This analysis requires a knowledge of the fine-structure splittings $^3P_{0,1,2}$ *vs.* $^1P_1$ and $^3F_{2,3,4}$ *vs.* $^1F_3$, respectively. Term energies are known up to high n for the $^1P_1$ and $^3P_2$ series [16]; however, information is available on the ^3F series only for $n \leq 13$. Thus, we have performed additional measurements on the fine structure in the F series for the predominant stable isotope ^{40}Ca, which is not affected by HFM, and have used this information to provide a detailed and accurate analysis of the HFS observed for the odd-mass isotopes.

2 Theory

The transition IS $\delta\nu_{AA'} = \nu_A - \nu_{A'}$ between two isotopes with masses M_A and $M_{A'}$ is caused by two effects: the change in nuclear mass and the change in nuclear charge distribution. Accordingly, the IS can be divided into two contributions: the mass shift (MS) and the field shift (FS)

$$\delta\nu_{AA'} = \delta\nu^{\mathrm{MS}}_{AA'} + \delta\nu^{\mathrm{FS}}_{AA'}. \tag{1}$$

The mass shift is given by

$$\delta\nu^{\mathrm{MS}}_{AA'} = K^{\mathrm{MS}}\,\frac{M_A - M_{A'}}{M_A M_{A'}}\,. \tag{2}$$

The mass shift constant K^{MS} is usually separated into the normal mass shift (NMS) constant K^{NMS}, due to change in the reduced mass, and the specific mass shift (SMS) constant K^{SMS}, caused by change in the correlation between electron momenta. While K^{NMS} can be calculated directly from the transition frequency ν, electron mass, and unit atomic mass,

$$K^{\mathrm{NMS}} = \frac{m_{\mathrm{e}}}{m_{\mathrm{u}}}\nu, \tag{3}$$

K^{SMS} is generally difficult to evaluate accurately. For transitions to a series of Rydberg states, the NMS has only a small n-dependence because of the small differences in the excitation energies. In our case, with n ranging from 13 to 40, the relative change in K^{NMS} is less than 1.2%. The SMS is also expected to be nearly independent of the final state since the Rydberg electron is at large mean radius and therefore should have only a very weak correlation with the core electrons. Thus, while there may be a SMS arising from changes in correlation when an electron is removed from the $4s$-orbital, it should be largely independent of the n of the final Rydberg state.

The first-order field shift is given by

$$\delta\nu^{\mathrm{FS}}_{AA'} = K^{\mathrm{FS}}\delta\left\langle r^2\right\rangle_{AA'}, \tag{4}$$

where $\delta\left\langle r^2\right\rangle_{AA'}$ is the change in mean-square nuclear charge radii and the FS constant is described in the non-relativistic approximation by

$$K^{\mathrm{FS}} = -\frac{Ze^2}{6\varepsilon_0}\Delta\left|\Psi\left(0\right)\right|^2. \tag{5}$$

Since the FS depends on the change in the electron probability density $\Delta\left|\Psi\left(0\right)\right|^2$ at the nucleus, it is generally significant only for transitions involving s-electrons. Similar to the SMS, there may be a FS due to removing an electron from the $4s$-orbital, but it should be independent of the particular final Rydberg state, since the probability density of a Rydberg electron at the nucleus is negligible.

Hyperfine structure is caused by coupling of electronic angular momenta with nuclear spin. In first order, the coupling can be described by a magnetic dipole interaction and an electric quadrupole interaction. For a particular hyperfine sublevel, identified by the hyperfine quantum

$$\begin{pmatrix} \langle S|W|S\rangle + E_S & \langle S|W|T^-\rangle & \langle S|W|T^0\rangle & \langle S|W|T^+\rangle \\ \langle T^-|W|S\rangle & \langle T^-|W|T^-\rangle + E_{T^-} & \langle T^-|W|T^0\rangle & \langle T^-|W|T^+\rangle \\ \langle T^0|W|S\rangle & \langle T^0|W|T^-\rangle & \langle T^0|W|T^0\rangle + E_{T^0} & \langle T^0|W|T^+\rangle \\ \langle T^+|W|S\rangle & \langle T^+|W|T^-\rangle & \langle T^+|W|T^0\rangle & \langle T^+|W|T^+\rangle + E_{T^+} \end{pmatrix}_F \tag{10}$$

number F, the energy shift induced by both effects is given by the Casimir formula

$$\Delta E_F = \frac{A}{2}C + \frac{B}{4}\frac{3C\,(C+1)/2 - 2I\,(I+1)\,J\,(J+1)}{(2I-1)\,(2J-1)\,IJ}, \tag{6}$$

where A is the magnetic dipole coupling constant, B is the electric quadrupole coupling constant, and C is composed from the state quantum numbers as

$$C = F(F+1) - J(J+1) - I(I+1).$$

Following the Breit-Wills formalism [17] for an atomic system with two valence electrons in an s,ℓ-configuration, the A and B coupling constants can be separated into contributions from the non-excited s-electron and the excited photoelectron. In the case of $s,n\ell$-Rydberg states, this description is greatly simplified because the contribution of the excited electron to the magnetic dipole interaction scales as $(n^*)^{-3}$ and the contribution to the electric quadrupole interaction scales as $(n^*)^{-6}$, where n^* is the effective principal quantum number. Hence, both can be assumed to be negligible for Rydberg states. Furthermore, the s-electron does not contribute to the quadrupole interaction so that the overall quadrupole coupling in an $s,n\ell$-Rydberg state can be taken as zero. Thus, the HFS in all four fine-structure components of an s,ℓ-configuration with $\ell \geq 1$ (singlet $^1\mathrm{L}_\ell$, and triplets $^3\mathrm{L}_{\ell-1}$, $^3\mathrm{L}_\ell$, and $^3\mathrm{L}_{\ell+1}$) can be described simply in terms of the unexcited s-electron magnetic dipole coupling:

$$\begin{aligned} A(S) &= a_s\left(\frac{c_1^2}{2\ell} - \frac{c_2^2}{2\ell+2}\right), \\ A(T^+) &= \frac{a_s}{2\ell+2},\ A(T^-) = -\frac{a_s}{2\ell}, \\ \text{and } A(T^0) &= a_s\left(\frac{c_2^2}{2\ell} - \frac{c_1^2}{2\ell+2}\right), \end{aligned} \tag{7}$$

where S denotes the singlet level, and T^+, T^0, and T^- denote the triplet levels with $J = \ell+1$, ℓ, and $\ell-1$, respectively. With pure Russell-Saunders (RS) coupling, the mixing coefficients c_1 and c_2 are given by

$$c_1 = \sqrt{\frac{\ell}{2\ell+1}} \text{ and } c_2 = \sqrt{\frac{\ell+1}{2\ell+1}}\,. \tag{8}$$

However, pure RS coupling may not be completely valid, and singlet and triplet terms with $J = \ell$ can mix to a certain degree. This mixing causes a small energy shift of both the S and T^0 levels, which can be observed as a shift of the T^0 level relative to the position of T^+ and T^-, as given by the Landé interval rules. Accordingly, the mixing coefficients c_1 and c_2 can be derived from a precise measurement of the term energy of all four fine-structure levels [18]:

$$c_1 = \sin\left(\arcsin\sqrt{\frac{\ell}{2\ell+1}} - \arcsin\sqrt{\frac{\Delta}{D}}\right), \tag{9}$$

where Δ is the deviation of T^0 from the Landé position and D is the $S - T^0$ splitting; c_2 is then found from the normalization condition $c_1^2 + c_2^2 = 1$.

Within first-order perturbation theory, which yields the usual Casimir HFS formula (6), only the contribution of the original eigenstate of the unperturbed Hamiltonian itself is considered. This description is valid only if the energy shift caused by the perturbation is considerably smaller than the energy gap to other nearby states. However, for Rydberg states the fine-structure splitting decreases with increasing n and eventually becomes comparable to, or even smaller than, the hyperfine interaction energy, which is dominated by the unexcited electron (7) and remains essentially constant with n. Under these conditions, second-order HFS theory, which considers interaction between the various fine-structure levels, must be applied. The complete HFS energy matrix for an s,ℓ-configuration with $\ell \geq 1$ is

see matrix (10) above

where W represents the hyperfine interaction Hamiltonian. There is such a matrix that must be diagonalized for each possible value of the hyperfine quantum number F, resulting in the perturbed energy levels as the eigenvalues of the matrix.

The diagonal elements of (10) are given by the fine-structure term energy plus the first-order HFS energy given by (6) using A values from (7). The non-diagonal elements have been evaluated in detail including up to octupole contributions [19]. However, as discussed above, contributions from the Rydberg electron are negligible and the s-electron makes no contribution to moments higher than the dipole. Thus, we retain from [19] only those components involving the a_{4s} coupling of the s-electron and resulting off-diagonal elements become

$$\begin{aligned} \langle T^-|W|S\rangle &= -\frac{c_1\,a_{4s}}{4\ell} \\ &\quad\times\sqrt{\left[\ell^2 - (F-I)^2\right]\left[(F+I+1)^2 - \ell^2\right]}, \\ \langle T^0|W|S\rangle &= -\frac{c_1\,c_2\,a_{4s}}{2}C\left(\frac{1}{2\ell+2} + \frac{1}{2\ell}\right), \end{aligned}$$

$$\langle T^0 \,|W|\, T^- \rangle = \frac{c_2\, a_{4s}}{4\ell} \times \sqrt{\left[\ell^2 - (F-I)^2\right]\left[(F+I+1)^2 - \ell^2\right]},$$

$$\langle T^+ \,|W|\, S \rangle = \frac{c_2\, a_{4s}}{2(2\ell+2)} \times \sqrt{\left[(\ell+1)^2 - (F-I)^2\right]\left[(F+I+1)^2 - (\ell+1)^2\right]},$$

$\langle T^+ \,|W|\, T^- \rangle = 0$, and

$$\langle T^+ \,|W|\, T^0 \rangle = \frac{c_1\, a_{4s}}{2(2\ell+2)} \times \sqrt{\left[(\ell+1)^2 - (F-I)^2\right]\left[(F+I+1)^2 - (\ell+1)^2\right]}. \quad (11)$$

The number of parameters required for the calculation of the HFS energy levels in this simplified model is reduced to five. These are a_{4s} and the four unperturbed fine-structure level energies. The latter are used in the diagonal elements, as well as to calculate the mixing coefficients c_1 and c_2, and can be taken from an even-mass isotope, *e.g.*, ^{40}Ca. The a_{4s} value can be obtained from measurement of the HFS in the ground state of the singly charged ion, where only a single $4s$ valence electron is present. In the case of ^{43}Ca this splitting has been measured very precisely [20] to yield $a_{4s,43} = -806.40207160(8)$ MHz. To our knowledge, no direct measurement exists for ^{41}Ca, but the Larmor frequency ratio $\omega_{\rm L}(^{43}{\rm Ca})/\omega_{\rm L}(^{41}{\rm Ca}) = 0.826208(5)$ [21] and the existing value for ^{43}Ca yield $a_{4s,41} = -975.91(4)$ MHz.

As mentioned above, the parameters c_1 and c_2 can be obtained from the fine-structure splitting in the even-mass isotopes. However, measurements of the complete fine structure are limited [16]. In the $4snp$ P series, the term energies are known for the ^{1}P$_1$ and ^{3}P$_2$ components up to $n > 60$, but the ^{3}P$_0$ and ^{3}P$_1$ terms are known only up to $n = 8$ and 14, respectively. Similarly, for the $4snf$ F series, the ^{1}F$_3$ terms are known up to $n = 28$ but complete triplet structure for ^{3}F$_{2,3,4}$ is known only up to $n = 11$. Nonetheless, a good first estimation of the HFM can be obtained by assuming pure RS coupling and extrapolating known fine-structure splittings using a power law of the effective quantum number, *i.e.*, $\Delta E_{\rm fs} \propto (n^*)^\alpha$.

Figure 2 shows the predicted evolution of all HFS levels of ^{43}Ca relative to the respective unperturbed ^{3}P$_1$ (A) and ^{3}F$_3$ (B) levels over the range of n from 6 to 40, calculated with the previously described HFM theory, using pure RS coupling and the exponent $\alpha = -3$ to estimate fine-structure splitting. The dashed lines show the behavior in the absence of hyperfine interaction, *i.e.*, what would be expected for the even-mass isotopes. In both plots, the effect of the HFS induced mixing on the triplet states is clearly visible and quite complex with partial reversal of ordering and regrouping of the individual HFS components. The situation is different for the singlet levels, which are well separated from the triplet levels by the relatively large singlet-triplet splitting. The position of the singlet HFS levels relative to each other are only slightly changed, but as a group they are shifted to higher and higher energy with increasing n value, relative to the unperturbed singlet level. If IS are measured only in the singlet system, this energy offset will appear as an anomalous IS for odd-mass isotopes that increases with n and converges to the shift of the $F = I - 1/2$ hyperfine component of the ionic ground state.

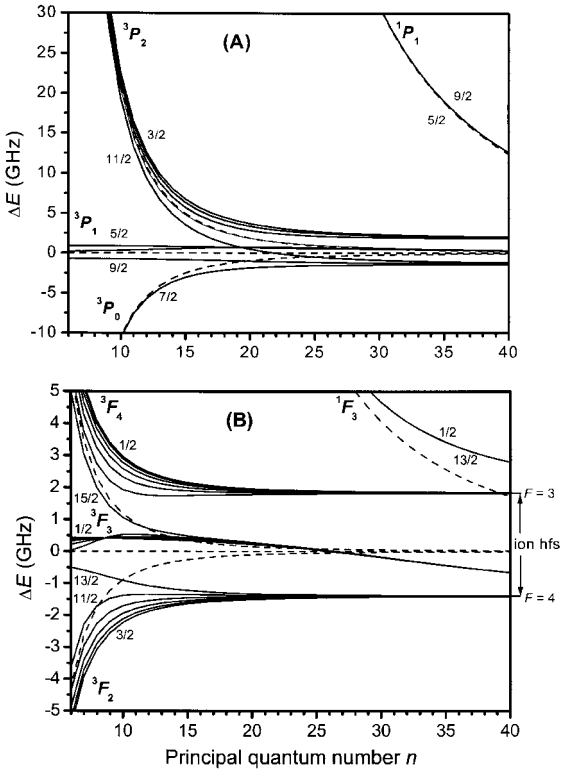

Fig. 2. Theoretical hyperfine structure in the (A) $4snp$ P and (B) $4snf$ F Rydberg series of ^{43}Ca as a function of principal quantum number n of the Rydberg electron. Minimum and maximum hyperfine F values are labeled for each fine-structure component and the dashed lines represent the fine-structure positions in the absence of HFM and HFS. Energies are given relative to the unperturbed middle triplet level, ^{3}P$_1$ and ^{3}F$_3$ respectively.

3 Experimental

The experimental apparatus has been described in detail in [4], so only a short overview is given here. Calcium is atomized in a resistively heated graphite furnace to produce a well-collimated beam of atoms. Most studies on the stable isotopes used a metallic calcium sample, while studies on radioactive ^{41}Ca were performed using aqueous nitrate solutions enriched to a ^{41}Ca/^{40}Ca ratio of $\sim 10^{-6}$. The atomic beam is irradiated perpendicularly by four laser beams, which sequentially cause the transitions shown by pathway C in Figure 1. The first transition at 422.8 nm is excited with a CW ring dye laser (Coherent 699-21)

using Stilbene 3 and pumped by an UV Ar-ion laser. For the second transition at 732.8 nm, a titanium-sapphire laser (Coherent 899-21) pumped by the 514.5 nm line of a second Ar-ion laser is used. The final resonant transitions to the Rydberg states are induced by an extended-cavity diode laser (EOSI 2010), which could be tuned from 835–885 nm. The two red lasers are counter-propagated against the 422.8 nm laser to give the best reduction of residual Doppler broadening. The Rydberg atoms are ionized by the 10.6 μm radiation from a CW CO_2 laser, which (in principle) allows ionization down to $n = 13$ in the P series and $n = 11$ in the F series. The resulting Ca^+ ions are mass filtered in a quadrupole mass spectrometer (QMS) and detected by a continuous dynode secondary electron multiplier.

All lasers used for resonant excitation steps are frequency stabilized by a computer-controlled system that evaluates the transmission fringes of each laser against those of a stabilized single-frequency He:Ne laser in a scanning Fabry-Perot interferometer (FPI) [22,23]. The residual frequency jitter of each laser is below 500 kHz and long-term drift is limited by that of the He:Ne laser at < 3 MHz/day. This system is capable of stabilizing the lasers at any arbitrary frequency and thus can also provide stabilized frequency scans and offset detunings. Since the free-spectral-range of the FPI is used for measuring frequency offsets, it has been calibrated against the ground state HFS in ^{133}Cs, resulting in a systematic scale uncertainty of 2×10^{-5}. Nonlinearity in the piezoelectric scanning of the FPI contributes another 100 kHz of systematic uncertainty. Day-to-day measurements of IS values in the same transition have shown an average reproducibility of about 1.2 MHz, which agrees well with expectations when statistical uncertainty of the line-fitting procedure is combined with the systematic uncertainties. The absolute frequencies of the lasers are monitored using a commercial wavemeter (Burleigh WA-1500) with an accuracy of 0.002 cm^{-1}, which was checked against the known frequency of the ^{133}Cs $6s\ ^2S_{1/2} \rightarrow 6p\ ^2P_{3/2}$ transition [24,25].

The long-wavelength limit of the diode laser used for the third excitation step dictated the lowest-lying Rydberg state that could be reached: $n = 15$ in the $^1P_1$ and $n = 13$ in the $^1F_3$ series. The shortest wavelength allowed excitation essentially up to the ionization limit (Rydberg $n = \infty$); however, the highest n studied was 40 because of other limiting factors, mainly DC-Stark effects resulting from the electric fields of the mass spectrometer ion extraction optics. To perform IS and HFS measurements in the Rydberg states, the first- and second-step lasers were tuned precisely to the center of the double-resonance condition for the predominant isotope ^{40}Ca, which could be found either by observing symmetric AC-Stark splitting with the intensity of one laser increased, or by two-dimensional scanning. A reference spectrum was then recorded by scanning the third-step laser over the ^{40}Ca resonance with the mass spectrometer set for mass 40. For each minor stable isotope, the QMS was set for the proper mass and the atomic beam intensity was adjusted to yield comparable signal strength for the different isotopic abundances, which vary over nearly 5 orders of magnitude. The first- and second-step lasers were tuned to resonance for the target isotope, using detunings obtained from previously measured IS and HFS data [4]. Then the third-step laser frequency was scanned over the same range used in the ^{40}Ca reference scan. The difference in the observed peak positions in the two scans corresponds to the $4s4d\ ^1D_2 \rightarrow Rydberg$ transition isotope shift (TIS). This result was converted to the level isotope shift (LIS), relative to the ground state, simply by adding the fixed first- and second-step detunings to the measured TIS. Measurements on ^{41}Ca followed a similar procedure, except that a discrete aqueous nitrate sample containing $\sim 4.5 \times 10^{12}$ atoms (0.3 ng) ^{41}Ca in a 10^6 excess of the stable isotopes was loaded into the atomization furnace. After drying and increasing the furnace temperature to slightly above the atomization threshold, the reference spectrum was recorded for ^{40}Ca. Then, after setting the first two lasers and the QMS for ^{41}Ca, repeated spectra were recorded while gradually increasing the furnace temperature until the sample was exhausted. The individual ^{41}Ca spectra were summed before analysis.

4 Results and discussion

Figure 3 shows typical sets of spectra recorded for excitation to the $4s16p\ ^1P_1$ and $4s16f\ ^1F_3$ Rydberg states. In the case of the odd-mass isotopes, state-selective excitation in the first two steps leads to population of only a single hyperfine level in the intermediate $4s4d\ ^1D_2$ state. It is favorable to choose strong transitions in the first two steps, *i.e.*, with $\Delta J = \Delta F$, leading to the $^1D_2$ ($F = 11/2$) state. However, selection rules ($\Delta F = 0, \pm 1$) dictate which hyperfine levels will be observed in the Rydberg state: from $^1D_2$ ($F = 11/2$), transitions to hyperfine levels with $F = 9/2$, $11/2$, and $13/2$ can be observed in the $^1F_3$ series, but only to the $F = 9/2$ level in the $^1P_1$ series. Therefore, in the latter case, we use the less favorable $^1D_2$ ($F = 7/2$) intermediate state to reach all hyperfine levels ($F = 5/2$, $7/2$, $9/2$) of the $^1P_1$ Rydberg states. These are visible as the three strong peaks in Figure 3A. The weak side-peaks arise from off-resonant excitation through other hyperfine levels in the intermediate $^1D_2$ state. Note that measurements for ^{41}Ca have been performed in the $^1F_3$ series only. This is because hyperfine-mixing effects are much more pronounced in the $^1F_3$ series, leading to more favorable IS for ultra-trace analysis. Also, optical pumping techniques [26] can be used to increase the excitation efficiency for odd-mass isotopes to $^1F_3$ states and make their response similar to that of even-mass isotopes.

The ^{43}Ca hyperfine components are clearly observed and well separated in the $^1P_1$ states (Fig. 3A), while in the $^1F_3$ state the splitting is smaller and the $\Delta F < \Delta J$ components are much weaker and only poorly resolved (Fig. 3B). All stable isotopes are observed at a level ~ 4 orders of magnitude above a flat background that arises from

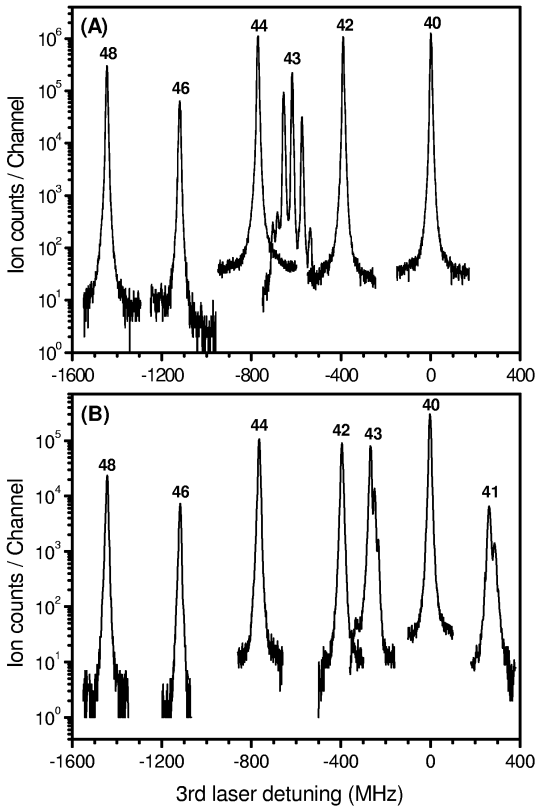

Fig. 3. Isotope shift measurements in the (A) $4s4d\ ^1\mathrm{D}_2 \rightarrow 4s16p\ ^1\mathrm{P}_1$ and (B) $4s4d\ ^1\mathrm{D}_2 \rightarrow 4s16f\ ^1\mathrm{F}_3$ transitions. Atomic beam current is adjusted to compensate for the natural abundance of each isotope, the first two lasers are fixed at their respective isotopic resonance frequencies while the third-step laser is scanned.

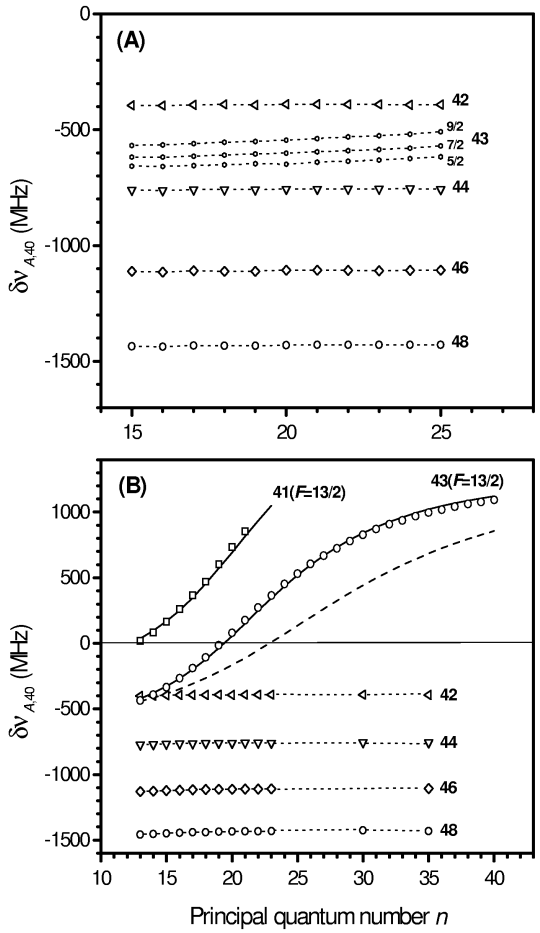

Fig. 4. Transition isotope shifts *versus* principal quantum number for the (A) $4snp\ ^1\mathrm{P}_1$ and (B) $4snf\ ^1\mathrm{F}_3$ Rydberg series. All three hyperfine components are shown for ^{43}Ca in the $^1\mathrm{P}_1$ series, while HFS is not resolved for ^{41,43}Ca in the $^1\mathrm{F}_3$ series on this scale and only the $F = 11/2 \rightarrow F = 13/2$ transitions are shown. The solid and dashed lines for ^{41,43}Ca are the results of HFM calculations discussed in the text.

the direct ionization of the $^1\mathrm{D}_2$ state by photons from either the first- or second-step laser. The background for ^{41}Ca is somewhat increased due to fast neutral particles and UV photons that are generated at the higher furnace temperature needed for complete atomization of the nitrate salt samples. In the spectra, all isotopes are well separated with linewidths of ~ 10 MHz (FWHM) and IS on the order of several hundred MHz. The even-mass isotopes exhibit a regular sequence of IS in both the $^1\mathrm{F}_3$ and $^1\mathrm{P}_1$ states, which can be attributed to the dominance of the NMS. In the $^1\mathrm{P}_1$ state, the center-of-gravity (cg) of the ^{43}Ca HFS appears to approximately follow this normal sequence. However, in the $^1\mathrm{F}_3$ state, the resonances for both ^{43}Ca and ^{41}Ca appear to be shifted to higher frequencies by ~ 400 MHz. This is a manifestation of strong hyperfine-induced fine-structure mixing and is discussed in detail below.

Spectra similar to those shown in Figure 3 were recorded for all members of the $^1\mathrm{P}_1$ series with $n = 15$ to 25. Within the $^1\mathrm{F}_3$ series, measurements for the even-mass isotopes were made for $n = 13$ to 23, as well as $n = 30$ and 35. For the odd-mass isotopes in the $^1\mathrm{F}_3$ series, ^{43}Ca was measured for all n values between 13 and 40, but ^{41}Ca was limited to $n = 13$ to 21 because of decreasing signal strength at higher n and the low abundance of the radioisotope. Resulting TIS values from these measurements are shown in Figure 4. In the $^1\mathrm{P}_1$ series the position of all three HFS components of ^{43}Ca are shown, while in the $^1\mathrm{F}_3$ series only the dominant $F = 11/2$ to 13/2 transitions for ^{41,43}Ca are given. LIS values for both series are listed in Tables 1 and 2. Numerical TIS values can be calculated from the tables by subtracting LIS values for the $4s4d\ ^1\mathrm{D}_2$ state given in [4]. Additionally, Rydberg term energies were obtained by summing the frequencies of the three resonant lasers when tuned for ^{40}Ca. For the $^1\mathrm{P}_1$ series, the resulting values are in reasonable agreement with those given in [16], although there is a small systematic difference, with our values consistently 0.07(1) cm^{-1} lower. Values for the $^1\mathrm{F}_3$ series are listed in Table 3 and for $n \leq 28$ they agree with previous measurements [27] to within ± 0.02 cm^{-1}, while those for $n = 29$ to 40 are determined for the first time.

As expected, the apparent IS for the even-mass isotopes exhibit very little change with Rydberg n and also little difference between the $^1\mathrm{P}_1$ and $^1\mathrm{F}_3$ series.

Table 1. Level isotope shifts in $4snp\ ^1P_1$ Rydberg states of calcium, relative to ^{40}Ca. The values for ^{43}Ca are given as the center-of-gravity of the hyperfine structure and the hyperfine magnetic dipole coupling constants A are also given (within uncertainty, $B = 0$ for all states). Estimated uncertainty for IS values is 1.2 MHz.

	Level isotope shift (MHz)					
n	^{42}Ca	^{43}Ca(cg)	$A(^{43}$Ca)	^{44}Ca	^{46}Ca	^{48}Ca
15	874.0	1314.3	11.3(1)	1685.3	2447.4	3146.4
16	876.0	1314.6	11.6(1)	1686.6	2449.8	3147.3
17	875.4	1319.8	11.9(1)	1687.1	2451.1	3148.0
18	877.7	1324.5	12.2(1)	1687.9	2450.4	3150.7
19	876.1	1328.4	12.0(1)	1687.2	2449.9	3149.2
20	877.5	1331.6	13.0(3)	1688.7	2453.5	3150.9
21	878.1	1338.8	12.8(1)	1689.4	2454.1	3152.7
22	878.5	1344.3	13.2(1)	1689.9	2454.6	3153.1
23	877.8	1349.1	13.1(1)	1691.4	2453.3	3153.9
24	877.1	1355.4	13.1(2)	1691.0	2455.2	3154.2
25	877.1	1365.2	13.6(6)	1688.8	2454.5	3155.1

Table 2. Level isotope shifts in the $4snf\ ^1F_3$ states of calcium, relative to ^{40}Ca. For ^{41,43}Ca the HFS is not completely resolved and the value given is for the predominant $F = 13/2$ level. Estimated uncertainty for all values is 1.2 MHz.

	Level isotope shift (MHz)					
n	^{41}Ca(13/2)	^{42}Ca	^{43}Ca(13/2)	^{44}Ca	^{46}Ca	^{48}Ca
13	620.0	869.4	1401.5	1674.4	2432.4	3124.5
14	682.4	868.6	1446.3	1675.8	2434.6	3128.7
15	763.2	874.8	1503.6	1679.4	2439.5	3133.8
16	860.6	875.5	1570.9	1683.0	2443.1	3138.1
17	966.5	875.1	1647.2	1683.4	2445.4	3142.5
18	1069.9	876.0	1730.5	1685.4	2448.0	3143.5
19	1202.3	877.1	1823.0	1687.2	2449.4	3145.7
20	1333.2	876.0	1917.0	1685.8	2449.6	3147.3
21	1453.7	876.6	2013.8	1687.6	2450.9	3149.5
22		877.2	2110.4	1688.2	2451.8	3149.9
23		877.8	2202.6	1686.3	2452.1	3151.1
24			2289.0			
25			2367.4			
26			2442.8			
27			2506.0			
28			2562.3			
29			2616.7			
30		878.1	2664.4	1691.0		3157.1
31			2707.5			
32			2744.1			
33			2774.6			
34			2805.6			
35		875.7	2834.1	1690.1	2453.8	3151.2
36			2857.1			
37			2878.4			
38			2899.5			
39			2914.9			
40			2929.8			

Table 3. Term energies of the $4snf\ ^1\mathrm{F}_3$ Rydberg series and fine-structure splittings to the $4snf\ ^3\mathrm{F}_{2,3,4}$ states of calcium. The $^1\mathrm{F}_3$ term energies are absolute with uncertainty of 0.005 cm^{-1}. The fine-structure splittings for $^3\mathrm{F}_{2,3}$ are directly measured on ^{40}Ca, while $^3\mathrm{F}_4$ values are derived from analysis of hyperfine mixing in ^{43}Ca. The fine-structure splittings are all given relative to $^1\mathrm{F}_3$ with an uncertainty < 0.0001 cm^{-1}.

	Term energy ($^1\mathrm{F}_3$, cm^{-1})		Fine-structure splitting (cm^{-1} from $^1\mathrm{F}_3$)		
n	this work	other [27]	$^3\mathrm{F}_2$	$^3\mathrm{F}_3$	$^3\mathrm{F}_4$
13	48647.318	48647.30	−0.6799	−0.6596	−0.6324
14	48738.551	48738.54			
15	48812.065	48812.09	−0.3899	−0.3762	−0.3577
16	48872.178	48872.20	−0.3052	−0.2938	−0.2783
17	48921.948	48921.95	−0.2433	−0.2336	−0.2205
18	48963.625	48963.67	−0.1967	−0.1885	−0.1774
19	48998.866	48998.89	−0.1615	−0.1544	−0.1450
20	49028.934	49028.93	−0.1342	−0.1280	−0.1198
21	49054.793	49054.80	−0.1127	−0.1075	−0.1004
22	49077.195	49077.20	−0.0955	−0.0907	−0.0843
23	49096.734	49096.74	−0.0822	−0.0781	
24	49113.869	49113.85	−0.0708	−0.0671	−0.0621
25	49128.981	49129.00			
26	49142.375	49142.38	−0.0538	−0.0508	−0.0468
27	49154.307	49154.29			
28	49164.977	49164.99	−0.0420	−0.0396	−0.0364
29	49174.561				
30	49183.199		−0.0338	−0.0319	−0.0295
31	49191.012				
32	49198.104				
33	49204.556				
34	49210.447				
35	49214.840				
36	49220.788				
37	49225.338				
38	49229.534				
39	49233.411				
40	49236.999				

However, these can be examined in more detail with Kingplot procedures using equations (1–4) and data on the change in mean-square nuclear charge radii from [28] to extract K^{SMS} and K^{FS}. The results of this analysis are shown in Figure 5. Within the measurement uncertainty, there appears to be no change in K^{FS} with respect to either n or ℓ of the Rydberg electron (Fig. 5A). This is not surprising since K^{FS} is proportional to the change in electron probability density at the nucleus, which should depend only on the removal of the electron from the $4s$-orbital, but not on the particular quantum numbers of the Rydberg state to which it is excited. The average value of $K^{\mathrm{FS}} = -106(3)$ MHz/fm^2 obtained for all the states studied here is, however, significantly different from the values of $-175.8(12)$ and $-179.5(22)$ MHz/fm^2 observed for the lower-lying $4s4p\ ^1\mathrm{P}_1$ and $4s4d\ ^1\mathrm{D}_2$ states [4], even though electrons in $4p$- and $4d$-orbitals should also have negligible probability of being at the nucleus. The large difference between the K^{FS} values for these two states and the Rydberg states must therefore be interpreted as a second-order effect where the excited $4p$- or $4d$-electron still interacts with the unexcited core and causes a significant reduction in the probability density of the remaining s-electrons at the nucleus.

In contrast to K^{FS}, the K^{SMS} values for the two Rydberg series (Fig. 5B) show a distinctly different behavior; there is very little change with n in the $^1\mathrm{F}_3$ series, while the $^1\mathrm{P}_1$ series shows a definite trend towards larger magnitude for higher n values. The nearly constant values in the $^1\mathrm{F}_3$ series are easily understood since first-order electron correlation occurs solely between electrons with a difference in orbital angular momentum of $\Delta\ell = \pm 1$ [29]. However, the Rydberg nf-electron has $\ell = 3$ while the remaining core contains only s- and p-electrons ($\ell = 0, 1$).

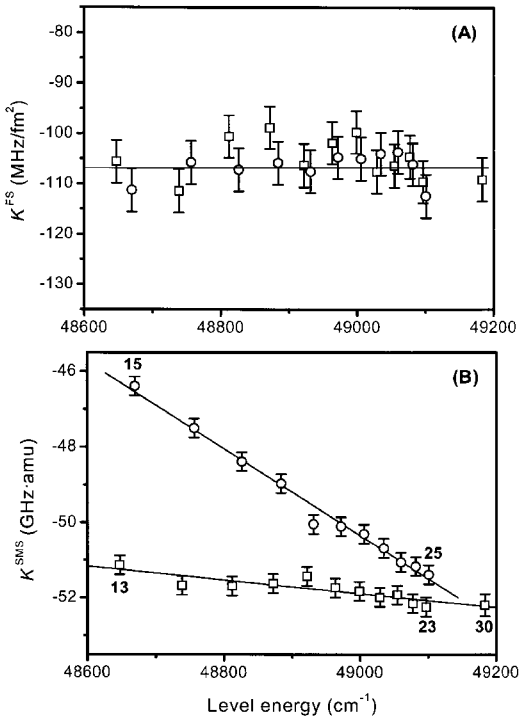

Fig. 5. (A) Field shift constants K^{FS} and (B) specific mass shift constants K^{SMS} derived from even-mass IS in the $4snp\ ^1P_1$ (circles) and $4snf\ ^1F_3$ (squares) Rydberg series as a function of term energy. Labels are the principal quantum number n. The line in (A) is the average value for all states. In (B) the lines are linear fits to the data, but are included only to guide the eye.

Thus, the average observed K^{SMS} of -52 GHz amu must be attributed to the change in the valence-core correlation when one of the ground state $4s$-electrons is removed. In contrast, the Rydberg np-electron of the $^1P_1$ series can correlate with the remaining $4s$-electron as well as other s-electrons in the core. However, this correlation diminishes as the Rydberg electron mean radius increases with n. It appears that for high n, where the correlation should disappear, the values for the $^1P_1$ series do approach those observed for the $^1F_3$ series.

While the IS values for the even-mass isotopes discussed above show only a very limited n-dependence, the behavior of the odd-mass isotopes is quite different. This is seen most clearly in the $^1F_3$ series for ^{43}Ca (Fig. 4B) where the apparent IS changes by more than 1.5 GHz as n increases from 13 to 40. As described in the theoretical section, this anomalous IS is attributed to the HFM. In Figure 4B, the dashed line is an *a priori* calculation of the position of the $F = 13/2$ hyperfine component. The HFM-induced shift was calculated using the known a_{4s} value, fine-structure splitting estimated from known term energies at $n = 10$ [16] scaled proportional to $(n^*)^{-3}$ with a constant quantum defect of 0.095, and assuming pure RS coupling. This corresponds to the difference between the $^1F_3$ ($F = 13/2$) position and the unperturbed $^1F_3$ position, as given respectively by the solid and dashed lines in the upper right corner of Figure 2B. The calculated shift shown in Figure 4B also includes the "normal" IS, which was calculated from equations (1−4) using the averaged $^1F_3$ series values of $K^{\mathrm{FS}} = -105.3(39)$ MHz/fm^2, $K^{\mathrm{SMS}} = -51.8(3)$ GHz amu, and $\delta\langle r^2\rangle_{43,40} = 0.113(3)$ fm^2 taken from [28]. The general trend of this *a priori* result agrees qualitatively with the experimentally measured shifts: at low n, where the fine-structure splitting is large, the agreement with experiment is good and approaches the "normal" IS value that would be expected in the absence of HFM. As n increases to high values, the IS increases and appears to approach the expected value of $-a_{4s}(2I+1)/2$ plus the "normal" IS. However, the transition between these two limits seems to be much slower in the calculation than in the experimental data. The most obvious interpretation of this discrepancy is that the HFM becomes stronger with increasing n more quickly than expected, which in turn would mean that the fine-structure splitting must decrease with n faster than expected. Thus, the calculation was repeated using the same constraints described above, except that the exponent of the fine-structure scaling ($\Delta E_{\mathrm{fs}} \propto (n^*)^{\alpha}$) was made a free parameter and adjusted by chi-square minimization to give the best fit between model and experiment. The result is shown as the solid line in Figure 4B and is obtained with the $n = 10$ fine-structure splitting scaled with $\alpha = -3.75$. It can be seen that this single parameter adjustment makes the agreement between model and experiment quite good. The *a priori* calculation was applied for ^{41}Ca using the new fine-structure scaling ($\alpha = -3.75$), $a_{4s,41} = -975.91$ MHz, and $\delta\langle r^2\rangle_{41,40} = 0.003(2)$ fm^2 [8]. The results are also shown as a solid line in Figure 4B and give good agreement with the experimental data.

Although scaling the fine structure proportional to $(n^*)^{-3.75}$ appears to fit the experimental data quite well, it is significantly different from the expected integer dependence of $\alpha = -3$, which had successfully described similar effects in strontium [14]. To investigate this further, we directly measured unperturbed fine-structure splittings for the predominant even-mass isotope ^{40}Ca. A typical result is shown in Figure 6A. Starting from the $4s4d\ ^1D_2$ excited state, intersystem transitions to $4snf\ ^3F_{2,3}$ states are strongly spin forbidden in a light element like calcium and the observed intensities are ~ 5 orders of magnitude lower than the allowed transitions to the $4snf\ ^1F_3$ states. Thus, spectra were recorded at higher atomic beam flux in the region of the $^3F_{2,3}$ states and then the flux was reduced by $\sim 2-3$ orders of magnitude as the scan continued over the region of the allowed $^1F_3$ state. Also, transitions to the $4snf\ ^3F_4$ states could not be observed because, in addition to being spin forbidden, these are also forbidden due to $\Delta J = 2$. Altogether, ^{40}Ca fine-structure splittings have been measured for $n = 13$, 15 to 22, 24, 26, 28, and 30. The shifts of the $^3F_{2,3}$ levels relative to $^1F_3$ are given in Table 3, along with the term energies for the $^1F_3$ states. The power dependence on n^* can be determined from the slope of a log-log plot of the observed splitting *vs.* n^*, as shown in Figure 7. For the $^1F_3-{}^3F_3$ splitting, the obtained slope is $\alpha = -3.60(3)$ in reasonable agreement with the

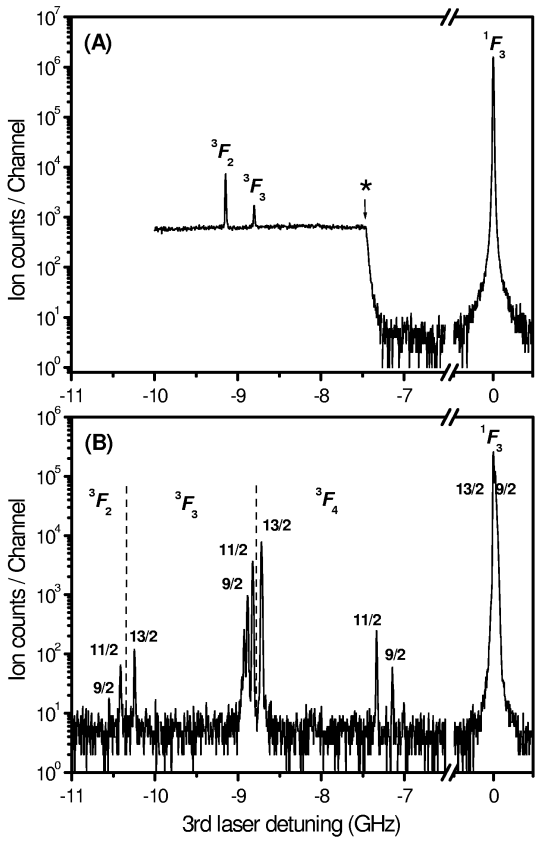

Fig. 6. (A) Measurement of fine-structure splitting for ^{40}Ca in $4s4d\ ^1\mathrm{D}_2 \rightarrow 4s16f$ F transitions; (∗) indicates where atomic beam current was reduced by a factor of ∼ 100. (B) Manifestations of hyperfine-induced mixing for ^{43}Ca in the same transitions; dotted vertical lines separate hyperfine groupings based on the fine-structure components of origin, as labeled.

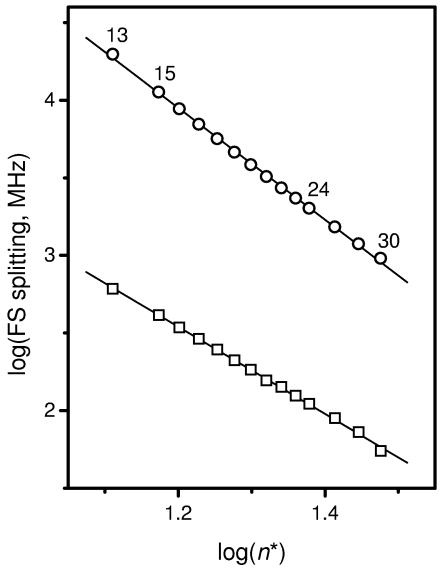

Fig. 7. Fine-structure splittings $\Delta E[^1\mathrm{F}_3{-}^3\mathrm{F}_3]$ (circles) and $\Delta E[^3\mathrm{F}_3{-}^3\mathrm{F}_2]$ (squares) in the $4snf$ Rydberg series of ^{40}Ca as a function of effective quantum number n^*. The slope of the lines gives the power dependence α in $\Delta E_{\mathrm{fs}} \propto (n^*)^{\alpha}$.

value of −3.75 obtained by fitting to the perturbed positions of $^1\mathrm{F}_3$ ($F = 13/2$) for ^{43}Ca. The observed power dependence for the $^3\mathrm{F}_3{-}^3\mathrm{F}_2$ splitting is considerably (and surprisingly) lower at $\alpha = -2.81(2)$; however, this has little effect on the perturbed positions of $^1\mathrm{F}_3$ for ^{43}Ca, which is dominated by the equal J $^1\mathrm{F}_3{-}^3\mathrm{F}_3$ mixing.

Our principal interest lies in understanding HFM and determining its contribution to the IS in the allowed $^1\mathrm{F}_3$ transition for ^{41,43}Ca and the corresponding influence on attainable isotopic selectivity. However, these HFM effects are even more strongly manifested in the triplet manifold. Figure 6B shows a typical spectrum obtained by scanning the third-step laser over a frequency range comparable to that in Figure 6A but with the QMS set at mass 43 and the first two lasers tuned for state selective excitation of the ^{43}Ca $4s4d\ ^1\mathrm{D}_2$ ($F = 11/2$) level. The observed structure corresponds to a vertical section in Figure 2 and several differences are immediately noticeable when comparing to the ^{40}Ca results in Figure 6A:

- transitions to the triplet states are much stronger. In the case of the $F = 13/2$ component at the center of the figure, it is only ∼ 1.5 orders of magnitude weaker than the $^1\mathrm{F}_3$ state. This is of course because singlet character is mixed into the triplet states and thus the transition becomes less forbidden. This trend continues as HFM becomes stronger at higher n and, at the highest state measured ($n = 30$), transitions to $^1\mathrm{F}_3$ and $^3\mathrm{F}_3$ have almost the same strength;
- transitions to components originating from $^3\mathrm{F}_4$ are now observed because, with HFM, J (as well as S) is no longer a good quantum number and only F remains valid for determining selection rules;
- the observed HFS splittings in the triplet manifold are much larger than in the singlet manifold. This is expected since under pure RS coupling there should be no HFS splitting in the $^1\mathrm{F}_3$ states. Even with HFM under pure RS coupling, the predicted $^1\mathrm{F}_3$ HFS splittings are < 5 MHz. The observed splittings of 10−30 MHz are slightly larger, indicating that there may be some deviations from pure RS coupling. With increasing n, the HFS levels converge so that only 4 lines are resolved, and finally at much higher n these 4 lines converge to the two HFS components of the ionic ground state (see Fig. 2).

Considering these observations, it is possible to reevaluate and/or to fit the theoretical model of HFM in greater detail. The unperturbed fine structure has been measured (except for $^3\mathrm{F}_4$) and can be used directly instead of an assumed power law. Similarly, HFS is well resolved and observed throughout the triplet manifold and thus provides much more data for fitting. Now the only free parameters to be fit are the unperturbed position of the $^3\mathrm{F}_4$ level and a reference frequency offset from the measured ^{40}Ca $^1\mathrm{F}_3$ position. The former completes a full set of fine-structure splittings and also defines the dependent subvariables c_1 and c_2, which are related to deviations from pure RS coupling. The latter simply corresponds to the "normal" IS

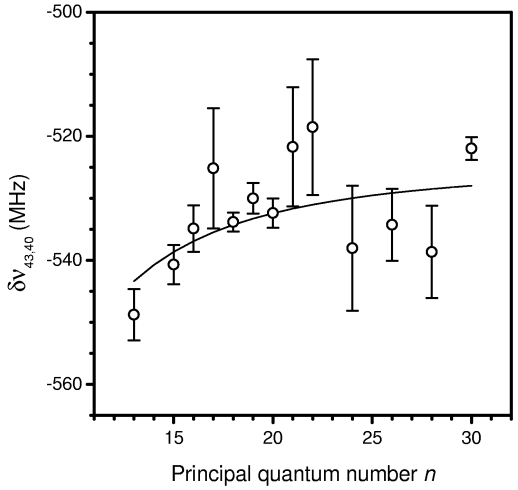

Fig. 8. Fit values for the "normal" isotope shift *versus* principal quantum number n for ^{43}Ca, derived from fits to spectra as shown in Figure 6B. The solid line is the IS calculated with averaged field shift and specific mass shift constants derived from the even-mass isotopes.

that would be observed in the absence of HFS and HFM. The derived $^3F_4$ fine-structure shifts are listed in Table 3 along with the measured shifts for $^3F_{2,3}$. The resulting values for the mixing coefficient c_1 show no distinct trend with n and the average value of 0.665(3) is only slightly greater than the pure RS value of 0.655. This is consistent with the small HFS splittings observed in the $^1F_3$ states and indicates that, in the absence of HFM, normal singlet-triplet mixing is quite small.

The fit offset values, corresponding to the "normal" IS, are plotted as points in Figure 8 and are compared to the values calculated with equations (1−4) using the averaged $K^{\rm FS}$ and $K^{\rm SMS}$ obtained from the King-plot analysis of the even-mass isotopes (solid line). Although there is some scatter in the values from the ^{43}Ca HFM analysis, the agreement between the two approaches is excellent with an average deviation of +1(7) MHz. The observed scatter in the HFM values is not too surprising since they are essentially derived from the determination of the center-of-gravity of complex, perturbed HFS that is spread out over 5−20 GHz.

Finally, similar HFM effects are expected for ^{41,43}Ca in the $^1P_1$ series; however, because the $^1P_1$−$^3P_1$ splitting is much larger than in the F series, the HFM becomes pronounced only at much higher n values. Over the range studied of up to $n = 25$, the observed HFS can still be treated as a normal first-order perturbation as given in (6). Further, for reasons already discussed, the quadrupole term can be taken as zero. Thus, the observed HFS can be simply fit with a magnetic dipole A parameter and an offset of the cg, corresponding to the apparent IS, both of which are listed for ^{43}Ca in Table 1. The cg does exhibit some HFM-induced shift away from the "normal" position predicted using the King-plot procedures. However, as expected, this shift is small, ranging from 11 MHz at $n = 15$ up to 59 MHz at $n = 25$.

5 Conclusions

Isotope shifts and hyperfine structure have been measured in the $4snp\ ^1P_1$ and $4snf$ F Rydberg series of calcium using high-resolution triple-resonance ionization mass spectrometry. Results have been obtained for all stable isotopes, including the 3×10^{-5} abundant ^{46}Ca, in both series. In addition, the radioisotope ^{41}Ca has been studied in the $^1F_3$ series. Analysis of IS data for the even-mass isotopes shows that, within experimental uncertainty, the field shift constants $K^{\rm FS}$ do not change with n and have nearly the same value for both the $^1P_1$ and $^1F_3$ series. In contrast, the specific mass shift constants $K^{\rm SMS}$ changes significantly with n in the $^1P_1$ series, but only slightly in the $^1F_3$ series, indicating that Rydberg p-electrons still have residual correlation with the unexcited core. HFS for the odd-mass isotopes ^{41,43}Ca was found to be increasingly perturbed as fine-structure splittings decrease and become comparable to the hyperfine interaction energy at higher n. These effects are particularly pronounced in the $4snf$ F series and cause anomalous isotope shifts of up to $\sim$ 1.5 GHz for the $^1F_3$ components. The observed ^{43}Ca spectra are well described by a second-order perturbation model of hyperfine-induced mixing of the fine-structure levels. In addition to the IS and HFS studies, new term energies have been measured in the $^1F_3$ series for $n = 29$−40 and fine-structure splittings between $^3F_3$, $^3F_2$ and $^1F_3$ have been measured for most members over the range $n = 13$−30. Furthermore, the $^3F_4$ splittings have been derived from the hyperfine-mixing model.

The existence of the n-dependent anomalous IS for ^{41}Ca is particularly important for analytical applications. The apparent transition isotope shift may be quite small, *e.g.*, at $n = 13$, but then increases to rather large values at higher n, and hence improves optical isotopic selectivity. However, excitation and ionization efficiencies decrease with increasing n and thus a judicious choice must be made to balance tradeoffs between sensitivity and selectivity. Combined with the isotopic selectivity of the first two transitions, it is estimated that triple-resonance optical selectivity for ^{41}Ca/^{40}Ca may be greater than 10^{11}. Initial experiments have indicated that under ideal circumstances ($n = 17$, all lasers below saturation intensity) optical selectivity of $\sim 10^{11}$ can indeed be reached; however, under conditions optimized for sensitivity ($n = 15$, all lasers near saturation intensity) this value is reduced by $\sim$ 2 orders of magnitude. Continuing work will evaluate the real analytical capabilities with respect to both selectivity and detection limits, and the lineshape model presented in [5] will be extended to the triple-resonance case for theoretical comparison.

The measurements reported in this work were performed at Pacific Northwest National Laboratory with support from the U.S. Department of Energy Office of Science under Contract DE-AC06-76RLO 1830. Additional support for P. Müller was provided by the "Zentrum für Umweltforschung der Johannes Gutenberg-Universität Mainz" and is gratefully acknowledged.

References

1. D. Fink, J. Klein, R. Middleton, Nucl. Instrum. Meth. Phys. Res. B **52**, 572 (1990).
2. S.P.H.T. Freeman, J.C. King, N.E. Vieira, L.R. Woodhouse, A.L. Yergey, Nucl. Instrum. Meth. Phys. Res. B **123**, 266 (1997).
3. K. Nishiizumi, J.R. Arnold, D. Fink, J. Klein, R. Middleton, Meteoritics **26**, 379 (1991).
4. W. Nörtershäuser, N. Trautmann, K. Wendt, B.A. Bushaw, Spectrochim. Acta B **53**, 709 (1998).
5. B.A. Bushaw, W. Nörtershäuser, K. Wendt, Spectrochim. Acta B **54**, 321 (1999).
6. B.A. Bushaw, Dissertation, Institut für Physik, Johannes Gutenberg-Universität Mainz, 1997.
7. B.A. Bushaw, Prog. Analyt. Spectrosc. **12**, 247 (1989).
8. C.W.P. Palmer, P.E.G. Baird, S.A. Blundell, J.R. Brandenberger, C.J. Foot, D.N. Stacey, G.K. Woodgate, J. Phys. B **17**, 2197 (1984).
9. K.-H. Weber, J. Lawrenz, K. Niemax, Phys. Scripta **34**, 14 (1986).
10. R. Beigang, K. Lücke, A. Timmermann, Phys. Rev. A **27**, 587 (1983).
11. R. Beigang, E. Matthias, A. Timmermann, Z. Phys. A **301**, 93 (1981).
12. H. Rinneberg, Z. Phys. A **302**, 363 (1981).
13. R. Beigang, A. Timmermann, Phys. Rev. A **26**, 2990 (1982).
14. B.A. Bushaw, H.-J. Kluge, J. Lantzsch, R. Schwalbach, J. Stenner, H. Stevens, K. Wendt, K. Zimmer, Z. Phys. D **28**, 275 (1993).
15. B.A. Bushaw, H.-J. Kluge, J. Lantzsch, R. Schwalbach, M. Schwarz, J. Stenner, H. Stevens, K. Wendt, K. Zimmer, in *Resonance Ionization Spectroscopy, Seventh International Symposium, Bernkastel-Kues, 1994*, edited by H.-J. Kluge, J.E. Parks, K. Wendt (AIP Conf. Proc. **329**, 1995), p. 381.
16. J. Sugar, C. Corliss, J. Phys. Chem. Ref. Data **8**, 865 (1979).
17. G. Breit, L.A. Wills, Phys. Rev. **44**, 470 (1933).
18. H. Kopfermann, *Kernmomente* (Akademische Verlagsgesellschaft, Frankfurt, 1956).
19. A. Lurio, M. Mandel, R. Novick, Phys. Rev. **126**, 1758 (1962).
20. F. Arbes, M. Benzing, T. Gudjons, F. Kurth, G. Werth, Z. Phys. D **31**, 27 (1994).
21. M. Arnold, J. Kowalski, T. Stehlin, F. Träger, G. zu Putlitz, Z. Phys. A **314**, 303 (1983).
22. B.A. Bushaw, B.D. Cannon, G.K. Gerke, T.J. Whitaker, Opt. Lett. **11**, 422 (1986).
23. W.Z. Zhao, J.E. Simsarian, L.A. Orozco, G.D. Sprouse, Rev. Sci. Instrum. **69**, 3737 (1998).
24. K.-H. Weber, C.J. Sansonetti, Phys. Rev. A **35**, 4650 (1987).
25. C.J. Sansonetti, C.-J. Lorenzen, Phys. Rev. A **30**, 1805 (1984).
26. P. Müller, B.A. Bushaw, K. Blaum, W. Nörtershäuser, N. Trautmann, K. Wendt, in *Resonance Ionization Spectroscopy, Ninth International Symposium, Manchester, 1998*, edited by J.C. Vickerman, I. Lyon, N.P. Lockyer, J.E. Parks (AIP Conf. Proc. **454**, 1998), p. 73.
27. S.A. Borgström, J.R. Rubbmark, J. Phys. B **10**, 3607 (1977).
28. G. Fricke, C. Bernhardt, K. Heilig, L.A. Schaller, L. Schellenberg, E.B. Shera, C.W. de Jager, At. Data Nucl. Data Tables **60**, 177 (1995).
29. E.R. Eliel, W. Hogervorst, T. Olsson, L.R. Pendrill, Z. Phys. A **311**, 1 (1983).